

Noninvasive Diagnosis of Nonalcoholic Fatty Liver Disease and Quantification of Liver Fat with Radiofrequency Ultrasound Data Using One-dimensional Convolutional Neural Networks

Aiguo Han, PhD • Michal Byra, PhD • Elhamy Heba, MD¹ • Michael P. Andre, PhD • John W. Erdman, Jr, PhD • Robit Loomba, MD, MHSc • Claude B. Sirlin, MD • William D. O'Brien, Jr, PhD

From the Bioacoustics Research Laboratory, Department of Electrical and Computer Engineering (A.H., W.D.O.), and Department of Food Science and Human Nutrition (J.W.E.), University of Illinois at Urbana-Champaign, 306 N Wright St, Urbana, IL 61801; Department of Radiology (M.B., M.P.A.), Liver Imaging Group, Department of Radiology (E.H., C.B.S.), and NAFLD Research Center, Division of Gastroenterology, Department of Medicine (R.L.), University of California, San Diego, La Jolla, Calif; and Department of Ultrasound, Institute of Fundamental Technological Research, Polish Academy of Sciences, Warsaw, Poland (M.B.). Received May 21, 2019; revision requested July 29; revision received December 2; accepted December 18. Address correspondence to A.H. (e-mail: han51@illinois.edu).

Supported by the National Institutes of Health (R01DK106419).

¹Current address: Department of Radiology, SUNY Upstate Medical University, Syracuse, NY.

Conflicts of interest are listed at the end of this article.

See also the editorial by Lockhart and Smith in this issue.

Radiology 2020; 00:1–9 • https://doi.org/10.1148/radiol.2020191160 • Content codes: GI IN US BQ

Background: Radiofrequency ultrasound data from the liver contain rich information about liver microstructure and composition. Deep learning might exploit such information to assess nonalcoholic fatty liver disease (NAFLD).

Purpose: To develop and evaluate deep learning algorithms that use radiofrequency data for NAFLD assessment, with MRI-derived proton density fat fraction (PDFF) as the reference.

Materials and Methods: A HIPAA-compliant secondary analysis of a single-center prospective study was performed for adult participants with NAFLD and control participants without liver disease. Participants in the parent study were recruited between February 2012 and March 2014 and underwent same-day US and MRI of the liver. Participants were randomly divided into an equal number of training and test groups. The training group was used to develop two algorithms via cross-validation: a classifier to diagnose NAFLD (MRI PDFF \geq 5%) and a fat fraction estimator to predict MRI PDFF. Both algorithms used one-dimensional convolutional neural networks. The test group was used to evaluate the classifier for sensitivity, specificity, positive predictive value, negative predictive value, and accuracy and to evaluate the estimator for correlation, bias, limits of agreements, and linearity between predicted fat fraction and MRI PDFF.

Results: A total of 204 participants were analyzed, 140 had NAFLD (mean age, 52 years \pm 14 [standard deviation]; 82 women) and 64 were control participants (mean age, 46 years \pm 21; 42 women). In the test group, the classifier provided 96% (95% confidence interval [CI]: 90%, 99%) (98 of 102) accuracy for NAFLD diagnosis (sensitivity, 97% [95% CI: 90%, 100%], 68 of 70; specificity, 94% [95% CI: 79%, 99%], 30 of 32; positive predictive value, 97% [95% CI: 90%, 99%], 68 of 70; negative predictive value, 94% [95% CI: 79%, 98%], 30 of 32). The estimator-predicted fat fraction correlated with MRI PDFF (Pearson r = 0.85). The mean bias was 0.8% (P = .08), and 95% limits of agreement were -7.6% to 9.1%. The predicted fat fraction was linear with an MRI PDFF of 18% or less (r = 0.89, slope = 1.1, intercept = 1.3) and nonlinear with an MRI PDFF greater than 18%.

Conclusion: Deep learning algorithms using radiofrequency ultrasound data are accurate for diagnosis of nonalcoholic fatty liver disease and hepatic fat fraction quantification when other causes of steatosis are excluded.

©RSNA, 2020

Online supplemental material is available for this article.

Nonalcoholic fatty liver disease (NAFLD) is the most common chronic liver disease worldwide, affecting approximately 25% of the human population (1). NAFLD covers a spectrum of liver abnormalities ranging from simple steatosis to nonalcoholic steatohepatitis. Hepatic steatosis, characterized by the accumulation of fat droplets within hepatocytes, can progress to nonalcoholic steatohepatitis, fibrosis, cirrhosis, and even hepatocellular carcinoma (1,2). Early detection and treatment may halt or reverse NAFLD progression (2). Liver biopsy remains the reference standard for diagnosing NAFLD and grading

hepatic steatosis. However, biopsy is costly, invasive, and inappropriate for screening.

There is a critical need to develop noninvasive imaging methods to assess hepatic steatosis. Several modalities have been investigated (3–8), among which MRI and conventional (qualitative) US have the advantage of involving no ionizing radiation. Confounder-corrected chemical shift-encoded MRI can measure the proton density fat fraction (PDFF), a leading method for noninvasive quantification of hepatic steatosis (4,5). However, chemical shift-encoded MRI is not routinely accessible. Conventional US is widely

Abbreviations

AUC = area under receiver operating characteristic curve, CI = confidence interval, CNN = convolutional neural network, NAFLD = non-alcoholic fatty liver disease, PDFF = proton density fat fraction, RF = radiofrequency, TGC = time gain compensation

Summary

When other causes of steatosis are excluded, de novo one-dimensional convolutional neural network algorithms can accurately identify nonalcoholic fatty liver disease and quantify hepatic fat fraction by using raw radiofrequency ultrasound data.

Key Results

- Deep learning with raw ultrasound data provided hepatic fat fraction estimates correlated to proton density fat fraction measured with confounder-corrected chemical shift-encoded MRI (Pearson $r = 0.85$).
- The proposed deep learning approach can diagnose nonalcoholic fatty liver disease (area under the receiver operating characteristic curve, 0.98) and is robust to changes in system settings, including transmit focal range and time gain compensation.

available for NALFD assessment but is limited by its qualitative nature, operator dependency, and modest accuracy (3).

Quantitative analysis of raw radiofrequency (RF) ultrasound signals shows potential for objective and accurate disease assessment (9). This analysis is based on the premise that by altering tissue microstructures, disease processes can cause quantifiable RF signal changes. Of note, the RF signals contain more information than do gray-scale B-mode images because information is lost or altered when B-mode images are generated from the raw data (9). Thus, when compared with B-mode images, the rich RF data may allow more comprehensive characterization of pathophysiologic conditions. By using a well-characterized phantom for system calibration, quantitative ultrasound techniques analyze the fundamental RF signals to extract system-independent parameters, such as the attenuation and backscatter coefficients, with minimal operator dependency (10–14). These coefficients are correlated with hepatic fat fraction (15–17).

To take further advantage of RF signals and to eliminate the dependency on a calibration phantom, we propose a phantom-free deep-learning ultrasound approach for objective, accurate, and automated NAFLD diagnosis and liver fat quantification. Deep learning (18,19) based on convolutional neural networks (CNNs) can extract features from raw data and has been applied to ultrasound B-mode image analysis (20–25) but not RF analysis for steatosis assessment. The current study developed and evaluated one-dimensional CNNs for NAFLD diagnosis and liver fat quantification using contemporaneous MRI PDFF as the reference standard. MRI PDFF was used because it accurately quantifies liver fat (4,5) and can be safely and ethically acquired in asymptomatic control participants.

Materials and Methods

Study Participants

This study was a secondary analysis of 204 prospectively enrolled adult research participants with NAFLD and control

participants without liver disease. The parent study was reported in a previous article (16) and used a different ultrasound analysis technique. For the current analysis, we developed and evaluated deep learning techniques in the same participants. The University of California, San Diego, approved this secondary analysis and the parent study, both of which complied with the Health Insurance Portability and Accountability Act. All participants provided written informed consent.

Participants were consecutively recruited by an expert hepatologist (R.L., >10 years of experience) from the University of California, San Diego, NAFLD Research Center between February 2012 and March 2014. Inclusion criteria were age of at least 18 years and willingness and ability to participate. Exclusion criteria were clinical, laboratory, or histologic evidence of a liver disease other than NAFLD; excessive alcohol consumption (>30 g per day within the past 10 years or >10 g per day in the previous year); and steatogenic or hepatotoxic medication use. NAFLD in study participants was defined as MRI PDFF of 5% or greater, with other causes of steatosis excluded (16). Control participants (MRI PDFF <5%) had no liver disease based on comprehensive clinical and laboratory testing performed under the supervision of and interpreted by the hepatologist. All participants underwent same-day US and chemical shift-encoded MRI of the liver.

Ultrasound Protocol

Nonenhanced US was performed by a research physician (E.H., 1 year of hands-on US training) using the 4C1 convex array (1–4 MHz) on a clinical ultrasound machine (Siemens S2000; Siemens, Issaquah, Wash) with an Ultrasound Research Interface option that allowed direct acquisition of RF data. Participants were positioned in the dorsal decubitus position, with the right arm at maximum abduction. The right liver lobe was visualized via a right intercostal approach, and a representative region of the parenchyma was identified, thereby avoiding major vasculature. The physician adjusted the transmit focal range and time gain compensation (TGC) (ie, a setting that reduces the effect of ultrasound attenuation on clinical images by increasing the received signal intensity with time [depth] [26]) for each participant, while fixing other settings. Ten consecutive RF frames were recorded at a rate of 10 frames per second when the participant was executing a breath hold in shallow expiration. Each frame had 560 lateral lines and was 10 cm deep. The machine automatically recorded the transmit focal range and the TGC settings (Appendix E1 [online]).

Ultrasound Data Preprocessing

A fixed region of interest with standard size and location (central 256 RF lines laterally; 1.8–9.7 cm axially) relative to the image frame was used for the one-dimensional CNN algorithms, yielding 2560 RF signals per participant (256 RF signals per frame \times 10 frames per participant). The region of interest was intended to cover as much of the liver region below the liver capsule as possible while generally avoiding tissues outside the liver. A fixed region of interest rather than a hand-drawn one tailored to each participant's liver anatomy was applied to minimize human intervention. No effort was made to

Table 1: Demographic, Physical, Biochemical, and MRI Proton Density Fat Fraction Characteristics of Study Participants

Characteristic	Training Group (<i>n</i> = 102)	Test Group (<i>n</i> = 102)	<i>P</i> Value
Men (%) [†]	40	38	.89
Age (y)*	51 ± 17	49 ± 17	.34
Height (cm)*	166 ± 10	167 ± 10	.38
Weight (kg)*	85 ± 21	84 ± 20	.81
BMI (kg/m ²)*	31 ± 6	30 ± 6	.43
Ethnic origin (%) [†]			.67
White	47	48	...
Hispanic	31	26	...
Asian	14	16	...
Black	4	4	...
Other	4	6	...
Diabetes [†]	42	47	.57
Biochemical profile*			
Hemoglobin (g/dL)	14 ± 2	14 ± 2	.09
Hematocrit (%)	40 ± 4	42 ± 4	.04
Platelet count (×10 ³ /µL)	251 ± 72	255 ± 66	.68
AST (U/L)	34 ± 27	34 ± 36	.95
ALT (U/L)	42 ± 37	44 ± 55	.81
Alkaline phosphatase (U/L)	76 ± 28	74 ± 23	.53
GGT (U/L)	45 ± 46	41 ± 45	.60
Total bilirubin (mg/dL)	0.5 ± 0.4	0.5 ± 0.3	.86
Albumin (g/dL)	4.5 ± 0.4	4.9 ± 3.9	.32
Glucose (mg/dL)	106 ± 47	110 ± 48	.52
Triglycerides (mg/dL)	145 ± 81	163 ± 275	.54
Total cholesterol (mg/dL)	183 ± 41	180 ± 46	.65
HDL cholesterol (mg/dL)	55 ± 21	54 ± 16	.72
LDL cholesterol (mg/dL)	101 ± 32	97 ± 30	.31
INR	1.0 ± 0.2	1.0 ± 0.2	.57
Imaging*			
MRI PDFF 5–8 (%)	11 ± 9	11 ± 8	.54

Note.—Unless otherwise noted, data are mean ± standard deviation. ALT = alanine aminotransferase, AST = aspartate aminotransferase, BMI = body mass index, GGT = γ-glutamyl transpeptidase, HDL = high-density lipoprotein, INR = international normalized ratio, LDL = low-density lipoprotein, PDFF = proton density fat fraction (mean calculated from segments 5–8). Table 1 is adapted and reprinted, with permission, from reference 16.

* Mean value provided with standard deviations and *P* values (*t* test). All laboratory results were obtained while patients were fasting.

[†] The χ² test *P* values are presented; note that the χ² test for comparing ethnic proportions in the two groups were conducted for white patients versus Hispanic patients versus Asian patients, black patients, and those with some other ethnicity.

completely exclude regions outside the liver, however, and the regions of interest contained variable amounts of extrahepatic tissue and structures.

Because TGC settings affect RF signals, quantitative analyses were performed before and after removal of the machine-recorded TGC settings.

The RF data of the last five frames were corrupted in two participants in the test group. The intact frames (frames 1–5) were duplicated for both participants to make 10 frames per participant for convenience of algorithm testing.

To reduce data size, the signals were downsampled by decimating the RF by four (ie, keeping every fourth sample) without filtering, to reduce the sampling frequency from 40 MHz to 10 MHz. According to the Nyquist-Shannon sampling theorem, the 10-MHz sampling frequency was sufficient to preserve useful information contained in the original signal acquired from

the 4C1 transducer (bandwidth, approximately 2–4 MHz). The downsampled signal containing 1024 sample points was input to the one-dimensional CNNs.

CNN Algorithm Development

Two one-dimensional CNN algorithms were developed: a binary classifier and a fat fraction estimator. For each RF signal input, the classifier output an NAFLD classification score between 0 and 1, and the fat fraction estimator output the predicted fat fraction as a percentage.

The participants were equally divided into training (*n* = 102) and test (*n* = 102) groups by using stratified randomization (16). The algorithms were developed by using the training group via cross-validation and were evaluated by using the test group. Details are presented in Appendix E2 (online), and the code is available for research use at <https://github.com/han51/naflf-1d-cnn>.

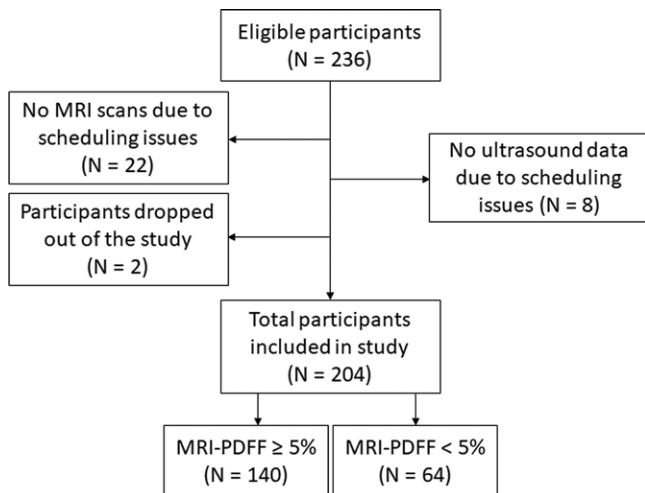


Figure 1: Flowchart of study participants included and excluded in the study, adapted from reference 16. PDFF = proton density fat fraction.

Statistical Analysis

Algorithms were evaluated at the participant level. Because each algorithm generated one output per RF signal input and because there were 2560 signal inputs per participant, the classifier and fat fraction estimator generated 2560 NAFLD classification scores and 2560 fat fraction estimates per participant, respectively. The 2560 outputs were averaged for each algorithm to yield composite per-participant scores and estimates. A cutoff of 0.5 for the composite score was set a priori for the NAFLD classifier.

To evaluate classifier performance, we calculated sensitivity, specificity, positive predictive value, negative predictive value, and overall accuracy for NAFLD identification in the test group. We also generated the receiver operating characteristic curve of the composite NAFLD classification score for the test group and calculated the area under the receiver operating characteristic curve (AUC) and the 95% confidence interval (CI). The DeLong test (27) was performed to compare the AUCs obtained by using signals without and with TGC.

To evaluate the fat fraction estimator performance, we calculated the correlation (Pearson r), bias, limits of agreement, and linearity between predicted fat fraction and MRI PDFF. Linearity was assessed by using sequential tests of polynomial fits to the plot of estimated fat fraction versus MRI PDFF (28). Linear range was identified if the linearity test over the entire MRI PDFF range failed. Linear regression slope, intercept, and R^2 were evaluated. Analyses were performed by using MATLAB R2016a (Mathworks, Natick, Mass) and RStudio 1.2 (RStudio, Boston, Mass) software. A P value less than .05 indicated statistical significance.

Results

Participant Characteristics

Participant characteristics are reported in Table 1. A total of 204 participants (Fig 1), 140 with NAFLD (mean age, 52 years \pm 14 [standard deviation]; 82 women) and 64 control participants (mean age, 46 years \pm 21; 42 women), were analyzed.

Men made up 40% (41 of 102) of the training group and 38% (39 of 102) of the test group. The mean body mass index was $31 \text{ kg/m}^2 \pm 6$ in the training group and $30 \text{ kg/m}^2 \pm 6$ in the test group. The mean MRI PDFF (segments 5–8) was $11\% \pm 9$ and $11\% \pm 8$ in the training and test groups, respectively. In each group, MRI PDFF ranged from 1% to 35%, and 70 of 102 participants (69%) had NAFLD ($\text{MRI PDFF} \geq 5\%$).

RF Signals and B-Mode Images

Representative B-mode images (with TGC) and RF signals are shown for two participants, referred to as participants A (MRI PDFF, 1%) (Fig 2) and B (MRI PDFF, 28%) (Fig 3). Figure 2a is a B-mode image reconstructed from frame 1 of the raw RF data (with TGC) acquired in participant A. The fixed region of interest is outlined by the superimposed yellow box. The blue dashed line is one of the 256 lines covered by the region of interest. The RF signals without and with TGC corresponding to the blue line in Figure 2a are shown in Figure 2b. Ultrasound attenuation with time (depth) was modest in the RF signal without TGC (Fig 2b), corresponding to the lower fat fraction. The TGC caused the deeper and weaker signals to be artificially more pronounced than the more superficial signals.

The reconstructed B-mode images were visually similar between adjacent frames (Fig 2a, 2c), although careful examination revealed differences that were likely due to slight motion between frames. In contrast, the RF signals along the same scan line (Fig 2d) were noticeably different between adjacent frames (eg, different intensities around 40, 70, and 95 μsec), both without and with TGC, as might be expected due to random and structured effects, which contributed to speckle and noise.

The reconstructed B-mode image and RF signals from participant B (Fig 3) visually differed from those from participant A (Fig 2a, 2b). The B-mode image was more homogeneous for participant B than for participant A. Blood vessels were visible on the B-mode image for participant A but were obscured for participant B. For the RF signals from participant B, increased attenuation with time (depth) was evident without TGC, corresponding to the higher fat fraction. The TGC compensated for this attenuation by increasing signal amplification with time.

Classification

In the test group, the composite NAFLD classification score provided a high degree of discrimination between control participants without liver disease and participants with NAFLD, as demonstrated by the receiver operating characteristic curves obtained by using RF signals without and with TGC (Fig 4). The AUCs were 0.98 (95% CI: 0.94, 1.00) and 0.95 (95% CI: 0.91, 0.99) for scores obtained by using RF signals without and with TGC, respectively. The two AUC estimates did not differ ($P = .23$).

Applying the predetermined threshold of 0.5 on the composite NAFLD classification score for NAFLD diagnosis in the test group yielded 68 true-positive results, two false-positive results, two false-negative results, and 30 true-negative results when RF signals without TGC were used and yielded 64

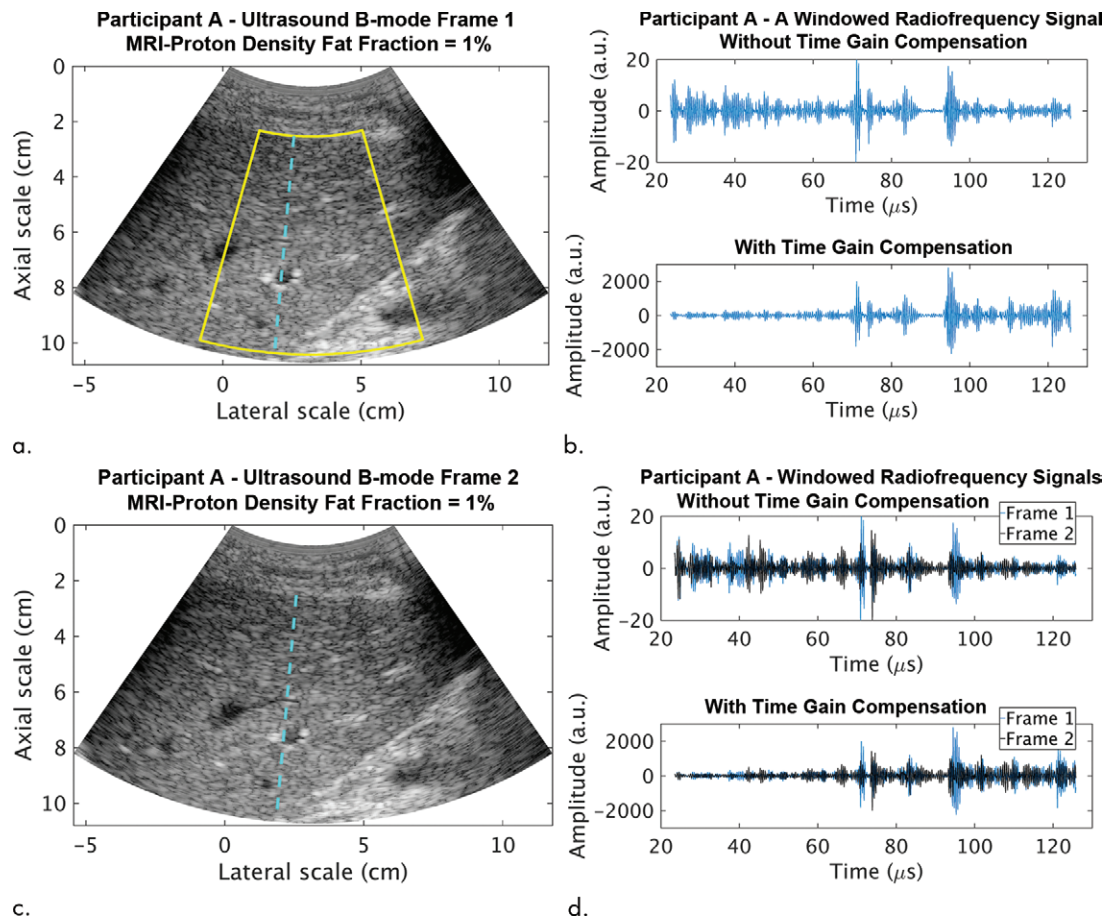


Figure 2: Data from 22-year-old woman with low proton density fat fraction (1%) (control participant, denoted participant A). Computer-reconstructed nonenhanced ultrasound B-mode images (sagittal plane with time gain compensation) and the underlying radiofrequency signals. **(a)** B-mode image frame 1 (with time gain compensation), with yellow outline superimposed to indicate the region of interest for deep learning analysis. **(b)** Radiofrequency signals corresponding to the blue line in **a**, without and with time gain compensation. **(c)** B-mode image frame 2 (with time gain compensation). **(d)** Radiofrequency signals corresponding to same location as indicated by the blue line in **c** but different frames (blue = frame 1, black = frame 2) without and with time gain compensation. Fixed region of interest includes signals from outside the liver.

true-positive results, four false-positive results, six false-negative results, and 28 true-negative results when RF signals with TGC were used. These diagnostic results yielded a classification accuracy of 96% in the test group using RF signals without TGC, with 97% sensitivity, 94% specificity, 97% positive predictive value, and 94% negative predictive value (Table 2). They yielded a classification accuracy of 90% in the test group using RF signals with TGC, with 91% sensitivity, 88% specificity, 94% positive predictive value, and 82% negative predictive value (Table 2).

Fat Fraction Estimation

The predicted fat fraction values correlated with the MRI PDFF in the test group for RF signals without and those with TGC (Fig 5). The Pearson correlation coefficient was 0.85 ($P < .001$) and 0.80 ($P < .001$) for use of RF signals without and with TGC, respectively.

Graphically, the predicted fat fraction versus MRI PDFF scatterplots (Fig 5) track the identity line. A linearity test (28) showed no nonlinearity between predicted fat fraction and MRI PDFF for MRI PDFF of 18% or less, regardless of whether TGC was removed. Linear regression of the predicted

fat fraction against MRI PDFF within the linear range (MRI PDFF $\leq 18\%$) yielded a slope of 1.1, an intercept of 1.3, and R^2 of 0.79 (Pearson $r = 0.89$) when signals without TGC were used and a slope of 0.9, an intercept of 3.1, and R^2 of 0.59 (Pearson $r = 0.77$) when signals with TGC were used. The fat fraction estimator underestimated the fat fraction for MRI PDFF greater than 18%, suggesting a saturation effect outside the linear range. Linear regression of the predicted fat fraction against MRI PDFF over the entire MRI PDFF range (MRI PDFF $< 35\%$) yielded a slope of 0.7, an intercept of 3.8, and R^2 of 0.73 (Pearson $r = 0.85$) when signals without TGC were used and a slope of 0.6, an intercept of 4.8, and R^2 of 0.64 (Pearson $r = 0.80$) when signals with TGC were used; the R^2 values were equal to the squared values of the Pearson correlation coefficients, as expected.

The mean bias of the predicted fat fraction over the entire MRI PDFF range was 0.8% ($P = .08$), and 95% limits of agreement were -7.6% to 9.1% when signals without TGC were used (Fig 6). When signals with TGC were used, the mean bias became 0.34% ($P = .49$), and the 95% limits of agreement were -9.4% to 10.0%.

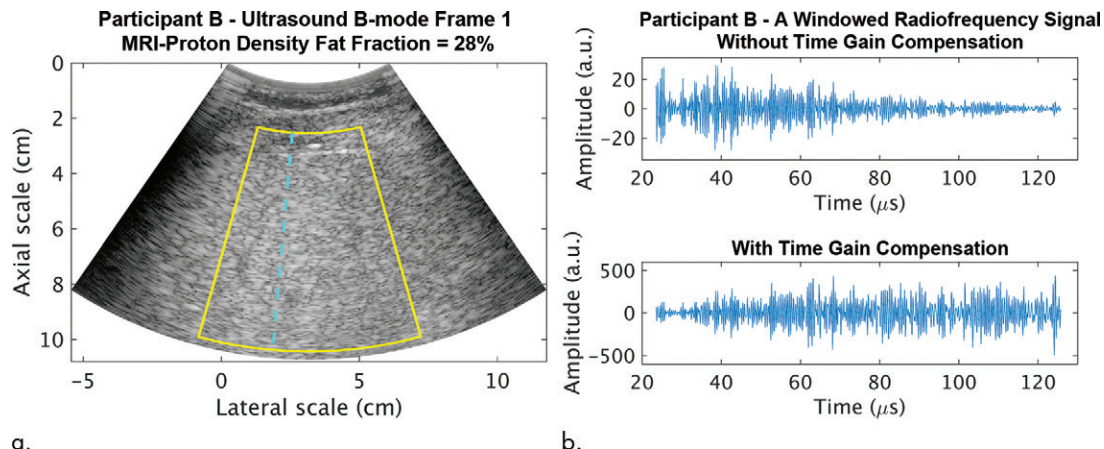


Figure 3: Data from 50-year-old man with high proton density fat fraction (28%) (participant with nonalcoholic fatty liver disease, denoted participant B). Computer-reconstructed nonenhanced ultrasound B-mode image (transverse plane with time gain compensation) and underlying radiofrequency signals. **(a)** B-mode image frame 1 for participant B, with yellow outline superimposed to indicate region of interest for deep learning analysis. **(b)** Radiofrequency signals corresponding to blue dashed line shown in **a**, without and with time gain compensation. Boundaries of the liver are not well delineated, and it is unclear whether the fixed region of interest includes signals from outside the liver.

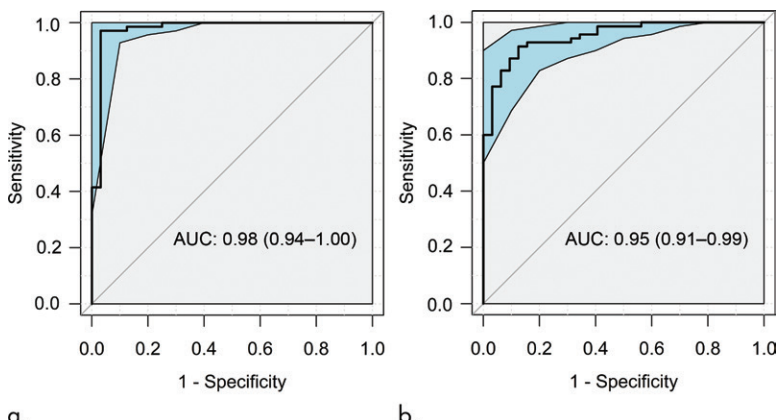


Figure 4: Receiver operating characteristic curves with 95% confidence bands of the composite nonalcoholic fatty liver disease classification scores yielded by the classifier for the test group using radiofrequency ultrasound signals **(a)** without and **(b)** with time gain compensation as the inputs. AUC = area under receiver operating characteristic curve.

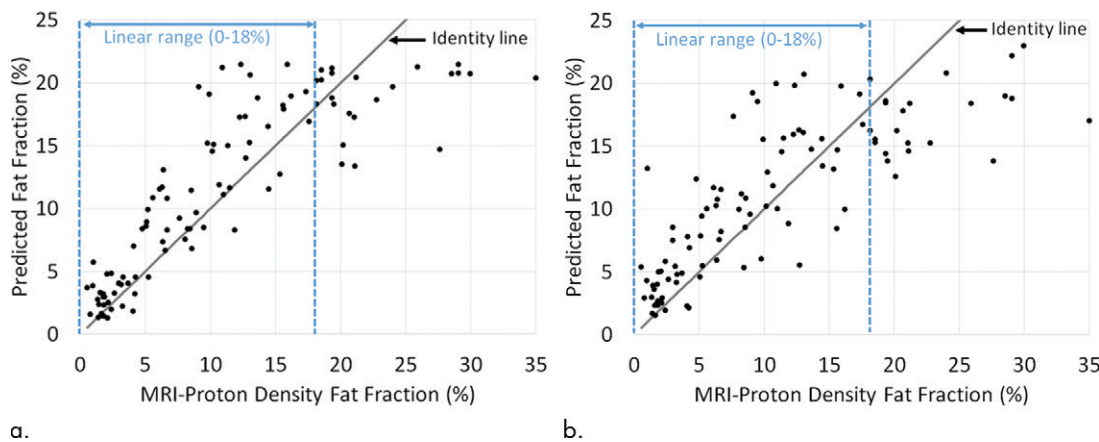
Table 2: Performance Metrics for Nonalcoholic Fatty Liver Disease Diagnosis in Test Group

Performance Metrics	Input: RF without TGC	Input: RF with TGC
Sensitivity	97 (90, 100) [68/70]	91 (82, 97) [64/70]
Specificity	94 (79, 99) [30/32]	88 (71, 96) [28/32]
PPV	97 (90, 99) [68/70]	94 (86, 98) [64/68]
NPV	94 (79, 98) [30/32]	82 (68, 91) [28/34]
Accuracy	96 (90, 99) [98/102]	90 (83, 95) [92/102]

Note.—Metrics were obtained by applying the predetermined threshold of 0.5 on the composite nonalcoholic fatty liver disease classification scores generated by the binary classifier. Values are expressed as percentages, with 95% confidence intervals in parentheses and fractions in square brackets. NPV = negative predictive value, PPV = positive predictive value, RF = radiofrequency, TGC = time gain compensation.

Discussion

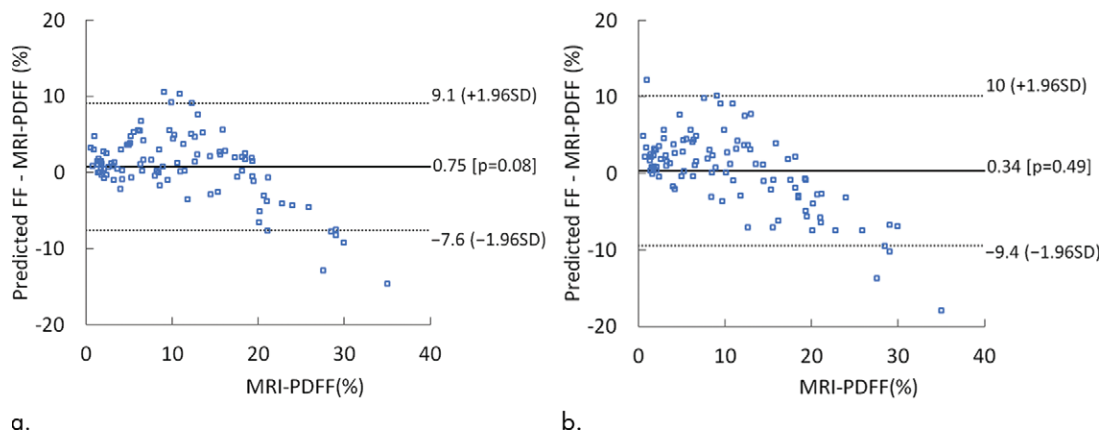
We developed one-dimensional convolutional neural network (CNN) algorithms for nonalcoholic fatty liver disease (NAFLD) diagnosis and fat fraction estimation using ultrasound radiofrequency (RF) signals as the input and MRI proton density fat fraction (PDFF) as the reference standard. The algorithms showed promising performance in a test group of 102 participants. The classifier yielded high classification accuracy (96%) and an area under the receiver operating characteristic curve of 0.98. The fat fraction estimator predicted fat fraction values that correlated with MRI PDFF ($r = 0.85$; $P < .001$) and that were linear with MRI PDFF over a broad range of clinically relevant MRI PDFF values. However, we also observed a possible saturation effect at MRI PDFF greater than 18%, the exact cause of which is not yet well understood. A potential explanation was insufficient training data for MRI PDFF greater than 18%. Another potential explanation was that ultrasonic signals could be insensitive to fat fraction changes at high MRI PDFF values. We also demonstrated the feasibility to develop and train one-dimensional CNNs de novo using RF signals, without using techniques, such as transfer learning (ie, reuse of a model pretrained on a different problem) and data augmentation (ie, artificial expansion of the input data through various transformations). We showed algorithm robustness under varying transmit focal range and time gain compensation (TGC) settings, although better performance was achieved by using signals without TGC. Other settings (eg, transmit frequency, line density) potentially critical to the algorithm performance were fixed. However, the model robustness with focal range and TGC suggested the one-dimensional CNN algorithms could be robust to more settings, possibly providing a phantom-free approach for ultrasound diagnosis using RF signals.



a.

b.

Figure 5: Predicted fat fraction versus MRI-derived proton density fat fraction obtained by using radiofrequency signals (a) without and (b) with time gain compensation. Blue lines represent the linear range. Gray line represents the identity line.



a.

b.

Figure 6: Difference between predicted fat fraction (FF) and MRI-derived proton density fat fraction (PDFF) versus the MRI-derived PDFF plots obtained by using radiofrequency signals (a) without and (b) with time gain compensation. SD = standard deviation.

Several studies have used deep learning with B-mode images for steatosis classification (Table 3). Byra et al (24) proposed a transfer learning approach to diagnose fatty liver disease using ultrasound B-mode images with a deep CNN pretrained with nonmedical images. They evaluated the approach in 55 patients with severe obesity, 38 of whom had fatty liver (with biopsy used as the reference standard), yielding 100% sensitivity, 88% specificity, 96% overall accuracy, and an AUC of 0.98. Reddy et al (25) used a similar transfer learning approach to diagnose fatty liver disease on 157 ultrasound liver images, with radiologists' qualitative score used as the ground truth, yielding 95% sensitivity, 85% specificity, 91% accuracy, and an AUC of 0.96. Although our classifier achieved performances nominally similar to those of Byra et al (24) and better than those of Reddy et al (25), it is difficult to directly compare the various studies because of differences in the reference and participant samples.

Several studies quantified liver steatosis by using MRI PDFF or liver biopsy as the reference standard (Table 3). For example, a study of 153 patients (29) showed that controlled attenuation parameter was correlated with the percentage of steatosis (Spearman $\rho = 0.47$), with biopsy used as the reference standard, and a study (30) in 107 participants showed a

0.57 Spearman correlation coefficient between the controlled attenuation parameter and MRI PDFF.

Use of RF signals has several potential advantages. Not only do RF signals contain more information than B-mode images (9) or the envelope data (Appendix E3 [online]), they are also less dependent on system settings and postprocessing operations or can be corrected for these, which can reduce variability. For instance, RF signals are not influenced by the dynamic range setting and filtering operations that affect the appearance of B-mode images. Additionally, diagnostic techniques based on RF signals are potentially more suitable for devices that do not easily produce B-mode images (eg, emerging wearable ultrasound devices [31]). Although training the one-dimensional CNN algorithms takes a considerable amount of time, the trained algorithms can be run in real time to analyze new data.

Our study had several limitations. First, the ultrasound data were acquired from a single scanner platform by one physician. The cross-platform and cross-operator generalizability of the algorithms remains to be tested. Second, the RF data are not yet readily available on all commercial ultrasound systems. However, more manufacturers are starting to provide RF capabilities. Third, this study did not address whether deep learning

Table 3: Summary of Ultrasound-based Studies on Fatty Liver Disease Diagnosis That Used Deep Learning and on Steatosis Quantification with Controlled Attenuation Parameter

Variable	Byra et al (24)	Reddy et al (25)	Myers et al (29)	Guthrie et al (30)
Task	Fatty liver disease diagnosis	Fatty liver disease diagnosis	Steatosis quantification	Steatosis quantification
Reference standard	Liver biopsy	Radiologists' qualitative score	Liver biopsy	MRI PDFF
Sample size	55 patients with severe obesity, 38 of whom had fatty liver disease	157 ultrasound liver images from unknown number of participants	153 patients	107 participants
Method	Deep learning with ultrasound B-mode images	Deep learning with ultrasound B-mode images	CAP	CAP
Results	Sensitivity, 100%; specificity, 88%; accuracy, 96%; AUC, 0.98	Sensitivity, 95%; specificity, 85%; accuracy, 91%; AUC, 0.96	Spearman $\rho = 0.47$ between CAP and biopsy-determined steatosis percentage	Spearman $\rho = 0.57$ between CAP and MRI PDFF

Note.—AUC = area under receiver operating characteristic curve, CAP = controlled attenuation parameter, PDFF = proton density fat fraction.

algorithms using RF data could outperform those using B-mode images. Finally, despite our efforts to provide methodologic details, other investigators might still have difficulty reproducing this deep learning study. To facilitate reproducibility, we have made our code available for research use.

A possible direction for future studies is to optimize the regions of interest to include only signals in the liver. The fixed region of interest used in this study was easy to implement and required no human intervention but included signals in a variable and uncontrolled manner from structures outside the liver, which probably reduced the algorithm performance. Another direction could be to assess the role of our algorithms in providing a cost-effective solution for quantifying longitudinal changes of liver fat in response to treatment.

In conclusion, one-dimensional convolutional neural network algorithms can be developed and trained de novo to accurately identify nonalcoholic fatty liver disease and quantify hepatic fat fraction using raw radiofrequency ultrasound data in the appropriate clinical context. The algorithms are robust to changes in several machine settings, including transmit focal range and time gain compensation.

Author contributions: Guarantors of integrity of entire study, A.H., W.D.O.; study concepts/study design or data acquisition or data analysis/interpretation, all authors; manuscript drafting or manuscript revision for important intellectual content, all authors; approval of final version of submitted manuscript, all authors; agrees to ensure any questions related to the work are appropriately resolved, all authors; literature research, A.H., M.P.A., R.L., C.B.S.; clinical studies, A.H., E.H., M.P.A., R.L., C.B.S.; experimental studies, A.H., M.P.A., W.D.O.; statistical analysis, A.H., M.B., W.D.O.; and manuscript editing, all authors

Disclosures of Conflicts of Interest: A.H. Activities related to the present article: disclosed no relevant relationships. Activities not related to the present article: institution received funding from Siemens Healthineers for the prior study. Other relationships: disclosed no relevant relationships. M.B. disclosed no relevant relationships. E.H. disclosed no relevant relationships. M.P.A. disclosed no relevant relationships. J.W.E. disclosed no relevant relationships. R.L. Activities related to the present article: received funding from NIEHS (5P42ES010337), NCATS (5UL1TR001442), NIDDK (R01DK106419, P30DK120515), and DOD PR-CRP (CA170674P2); received an investigator-initiated study grant from Siemens. Activities not related to the present article: disclosed no relevant relationships. Other relationships: is a consultant or advisory board member for Arrowhead Pharmaceuticals, AstraZeneca, Bird Rock Bio, Boehringer Ingelheim, Bristol-

Myer Squibb, Celgene, Cirius, CohBar, Conatus, Eli Lilly, Galmed, Gemphire, Gilead, Glymphase bio, GNI, GRI Bio, Intercept, Ionis, Janssen Inc., Merck, Metacrine, NGM Biopharmaceuticals, Novartis, Novo Nordisk, Pfizer, Prometheus, Sanofi, Siemens, and Viking Therapeutics; institution has received grant support from Allergan, Boehringer-Ingelheim, Bristol-Myers Squibb, Cirius, Eli Lilly, Galectin Therapeutics, Galmed Pharmaceuticals, GE, Genfit, Gilead, Intercept, Grail, Janssen, Madrigal Pharmaceuticals, Merck, NGM Biopharmaceuticals, NuSirt, Pfizer, pH Pharma, Prometheus, and Siemens; is the co-founder of Liponexus. C.B.S. Activities related to the present article: disclosed no relevant relationships. Activities not related to the present article: is on the board of the Society of Abdominal Radiology, AMRA, Guerbet, and Bristol Myers Squibb; is a consultant for GE Healthcare, Bayer, AMRA, Fulcrum Therapeutics, and IBM/Watson Health; institution received grants from Gilead, GE Healthcare, Siemens, GE MRI, Bayer, GE Digital, GE US, ACR Innovation, Philips, and Celgene; is a speaker for GE Healthcare and Bayer; institution receives royalties from Wolters Kluwer Health (UpToDate Publishing); developed educational presentations for Medscape and Resoundant; institution has lab service agreements with Enanta, ICON Medical Imaging, Gilead, Shire, Virtualscopics, Intercept, Synageva, Takeda, Genzyme, Janssen, NuSirt, Celgene-Parexel, and Organovo; has independent consulting contracts with Epigenomics and Blade Therapeutics; developed educational presentations or articles for Medscape. Other relationships: disclosed no relevant relationships. W.D.O. disclosed no relevant relationships.

References

1. Loomba R, Sanyal AJ. The global NAFLD epidemic. *Nat Rev Gastroenterol Hepatol* 2013;10(11):686–690.
2. Friedman SL, Neuschwander-Tetri BA, Rinella M, Sanyal AJ. Mechanisms of NAFLD development and therapeutic strategies. *Nat Med* 2018;24(7):908–922.
3. Machado MV, Cortez-Pinto H. Non-invasive diagnosis of non-alcoholic fatty liver disease. A critical appraisal. *J Hepatol* 2013;58(5):1007–1019.
4. Le TA, Chen J, Changchien C, et al. Effect of coleseviam on liver fat quantified by magnetic resonance in nonalcoholic steatohepatitis: a randomized controlled trial. *Hepatology* 2012;56(3):922–932.
5. Noureddin M, Lam J, Peterson MR, et al. Utility of magnetic resonance imaging versus histology for quantifying changes in liver fat in nonalcoholic fatty liver disease trials. *Hepatology* 2013;58(6):1930–1940.
6. Park CC, Nguyen P, Hernandez C, et al. Magnetic resonance elastography vs transient elastography in detection of fibrosis and noninvasive measurement of steatosis in patients with biopsy-proven nonalcoholic fatty liver disease. *Gastroenterology* 2017;152(3):598–607.e2.
7. Reeder SB, Cruite I, Hamilton G, Sirlin CB. Quantitative assessment of liver fat with magnetic resonance imaging and spectroscopy. *J Magn Reson Imaging* 2011;34(4):729–749.
8. Artz NS, Hines CDG, Brunner ST, et al. Quantification of hepatic steatosis with dual-energy computed tomography: comparison with tissue reference standards and quantitative magnetic resonance imaging in the ob/ob mouse. *Invest Radiol* 2012;47(10):603–610.
9. Oelze ML, Mamou J. Review of quantitative ultrasound: envelope statistics and backscatter coefficient imaging and contributions to diagnostic ultrasound. *IEEE Trans Ultrason Ferroelectr Freq Control* 2016;63(2):336–351.
10. Han A, Andre MP, Erdman JW Jr, Loomba R, Sirlin CB, O'Brien WD Jr. Repeatability and reproducibility of a clinically based QUS phantom study and methodologies. *IEEE Trans Ultrason Ferroelectr Freq Control* 2017;64(1):218–231.
11. Han A, Andre MP, Deiranieh L, et al. Repeatability and reproducibility of the ultrasonic attenuation coefficient and backscatter coefficient measured in the right lobe

- of the liver in adults with known or suspected nonalcoholic fatty liver disease. *J Ultrasound Med* 2018;37(8):1913–1927.
12. Han A, Labyed Y, Sy EZ, et al. Inter-sonographer reproducibility of quantitative ultrasound outcomes and shear wave speed measured in the right lobe of the liver in adults with known or suspected non-alcoholic fatty liver disease. *Eur Radiol* 2018;28(12):4992–5000.
 13. Han A, Zhang YN, Boehringer AS, et al. Inter-platform reproducibility of ultrasonic attenuation and backscatter coefficients in assessing NAFLD. *Eur Radiol* 2019;29(9):4699–4708.
 14. Yao LX, Zagzebski JA, Madsen EL. Backscatter coefficient measurements using a reference phantom to extract depth-dependent instrumentation factors. *Ultrason Imaging* 1990;12(1):58–70.
 15. Andre MP, Han A, Heba E, et al. Accurate diagnosis of nonalcoholic fatty liver disease in human participants via quantitative ultrasound. 2014 IEEE International Ultrasonics Symposium, Chicago, September 3–6, 2014. Piscataway, NJ: IEEE, 2014; 2375–2377.
 16. Lin SC, Heba E, Wolfson T, et al. Noninvasive diagnosis of nonalcoholic fatty liver disease and quantification of liver fat using a new quantitative ultrasound technique. *Clin Gastroenterol Hepatol* 2015;13(7):1337–1345.e6.
 17. Paige JS, Bernstein GS, Heba E, et al. A pilot comparative study of quantitative ultrasound, conventional ultrasound, and MRI for predicting histology-determined steatosis grade in adult nonalcoholic fatty liver disease. *AJR Am J Roentgenol* 2017;208(5):W168–W177.
 18. LeCun Y, Bengio Y, Hinton G. Deep learning. *Nature* 2015;521(7553):436–444.
 19. Esteva A, Kuprel B, Novoa RA, et al. Dermatologist-level classification of skin cancer with deep neural networks. *Nature* 2017;542(7639):115–118 [Published correction appears in *Nature* 2017;546(7660):686.]
 20. Han S, Kang HK, Jeong JY, et al. A deep learning framework for supporting the classification of breast lesions in ultrasound images. *Phys Med Biol* 2017;62(19):7714–7728.
 21. Xu Y, Wang Y, Yuan J, Cheng Q, Wang X, Carson PL. Medical breast ultrasound image segmentation by machine learning. *Ultrasonics* 2019;91:1–9.
 22. Yap MH, Pons G, Martí J, et al. Automated breast ultrasound lesions detection using convolutional neural networks. *IEEE J Biomed Health Inform* 2018;22(4):1218–1226.
 23. Byra M, Galperin M, Ojeda-Fournier H, et al. Breast mass classification in sonography with transfer learning using a deep convolutional neural network and color conversion. *Med Phys* 2019;46(2):746–755.
 24. Byra M, Styczynski G, Szmigelski C, et al. Transfer learning with deep convolutional neural network for liver steatosis assessment in ultrasound images. *Int J CARS* 2018;13(12):1895–1903.
 25. Reddy DS, Bharath R, Rajalakshmi P. A novel computer-aided diagnosis framework using deep learning for classification of fatty liver disease in ultrasound imaging. 2018 IEEE 20th International Conference on e-Health Networking, Applications and Services (Healthcom), Ostrava, Czech Republic, September 17–20, 2018. Piscataway, NJ: IEEE, 2018.
 26. Reid JM, Wild JJ. Ultrasonic ranging for cancer diagnosis. *Electronics (Basel)* 1952;25(5):136–138.
 27. DeLong ER, DeLong DM, Clarke-Pearson DL. Comparing the areas under two or more correlated receiver operating characteristic curves: a nonparametric approach. *Biometrics* 1988;44(3):837–845.
 28. Raunig DL, McShane LM, Pennello G, et al. Quantitative imaging biomarkers: a review of statistical methods for technical performance assessment. *Stat Methods Med Res* 2015;24(1):27–67.
 29. Myer RP, Poller A, Kirsch R, et al. Controlled attenuation parameter (CAP): a noninvasive method for the detection of hepatic steatosis based on transient elastography. *Liver Int* 2012;32(6):902–910.
 30. Guthrie H, Castro N, Beysen C, Morrow L, Hompesch M. Relationship between controlled attenuation parameter (CAP) and magnetic resonance imaging-derived proton density fat fraction (MRI-PDFF) in subjects at high risk for nonalcoholic fatty liver disease (NAFLD). ProSciento, Inc. https://prosciento.com/wp-content/uploads/2019/02/NASHTAG2019-Poster_Hompesch_FINAL-CB12292018L.pdf. Accessed April 23, 2019.
 31. Wang C, Li X, Hu H, et al. Monitoring of the central blood pressure waveform via a conformal ultrasonic device. *Nat Biomed Eng* 2018;2(9):687–695.